

Extensive near-infrared (*H*-band) photometry in Coma^{*}

S. Andreon¹, R. Pelló², E. Davoust², R. Domínguez^{2,3}, and P. Poulain²

¹ Osservatorio Astronomico di Capodimonte, via Moiariello 16, 80131 Napoli, Italy
e-mail: andreon@na.astro.it

² Observatoire Midi-Pyrénées, LAT, UMR 5572, 14 Av. E. Belin, F-31400 Toulouse, France
e-mail: roser,davoust,poulain@obs-mip.fr

³ Departament d'Astronomia i Meteorologia, Martí i Franquès 1, 08028 Barcelona, Spain

Received June 16; accepted October 6, 1999

Abstract. We present extensive and accurate photometry in the near-infrared *H* band of a complete sample of objects in an area of about 400 arcmin² toward the Coma cluster of galaxies. The sample, including about 300 objects, is complete down to $H \sim 17$ mag, the exact value depending on the type of magnitude (isophotal, aperture, Kron) and the particular region studied. This is six magnitudes below the characteristic magnitude of galaxies, well into the dwarfs' regime at the distance of the Coma cluster. For each object (star or galaxy) we provide aperture magnitudes computed within five different apertures, the magnitude within the 22 mag arcsec⁻² isophote, the Kron magnitude and radius, magnitude errors, as well as the coordinates, the isophotal area, and a stellarity index. Photometric errors are 0.2 mag at the completeness limit. This sample is meant to be the zero-redshift reference for evolutionary studies of galaxies.

Key words: galaxies: luminosity function, mass function
— galaxies: clusters: individual: Coma (=Abell 1656)

1. Introduction

Our present knowledge of the near-infrared properties of galaxies is still very sketchy, because panoramic astronomical imaging receivers in that domain have only been available recently. For samples complete in the near-infrared band, properties such as galaxian colors and sizes in the near-infrared and their dependence on morphological type are almost unknown. And so are the deep near-infrared luminosity functions of galaxies in the field and in clusters. The former have been investigated by Gardner et al.

(1997) and, for an optically-selected sample, by Szokoly et al. (1998), but they cover just its bright end. The latter concern the bright end of intermediate-distance clusters (Trentham & Mobasher 1998; Barger et al. 1996); an exception is the study of the luminosity function of the center of Coma by de Propris et al. (1998), which reaches $H \sim 16$ mag (at 80% completeness).

Near-infrared properties of galaxies are very useful for a number of projects. These quantities allow the determination of a possible change with redshift in the galaxy properties, such as the “downsizing” suggested by Cowie et al. (1996). The passband dependence, from the optical to the near-infrared, of the tilt of the fundamental plane gives a clear indication of whether this tilt is due to a variation of metallicity, age or a breakdown in homology along the early-type sequence (Pahre et al. 1998), but the fundamental plane in the near-infrared is only beginning to be studied. The existence of dwarf galaxies with blue $B - K$ colors has been assumed, in order to explain galaxy counts in B and K (Saracco et al. 1996), but their density in the universe still has to be measured.

Near-infrared measurement of nearby galaxies and clusters are valuable, because even at high redshift the near-infrared falls into a well known part of the restframe spectrum, at the difference of the optical window, which, at high redshift, samples the almost unexplored restframe ultraviolet emission. In passing, the galaxy size distribution plays a fundamental role in performing new cosmological tests (Petrosian 1998). Their determination in the present Universe is critical for these tests.

In short, good reference samples of galaxies with well established spectrophotometric properties – from the optical to the near-infrared – are urgently needed for the study of galaxy properties and their evolution.

We thus started a program to establish the near-infrared photometric properties of galaxies in Coma, the archetypical zero-redshift cluster, for which a large

^{*} Based on observations collected with the Telescope Bernard Lyot, at the Pic du Midi Observatory, operated by INSU (CNRS).

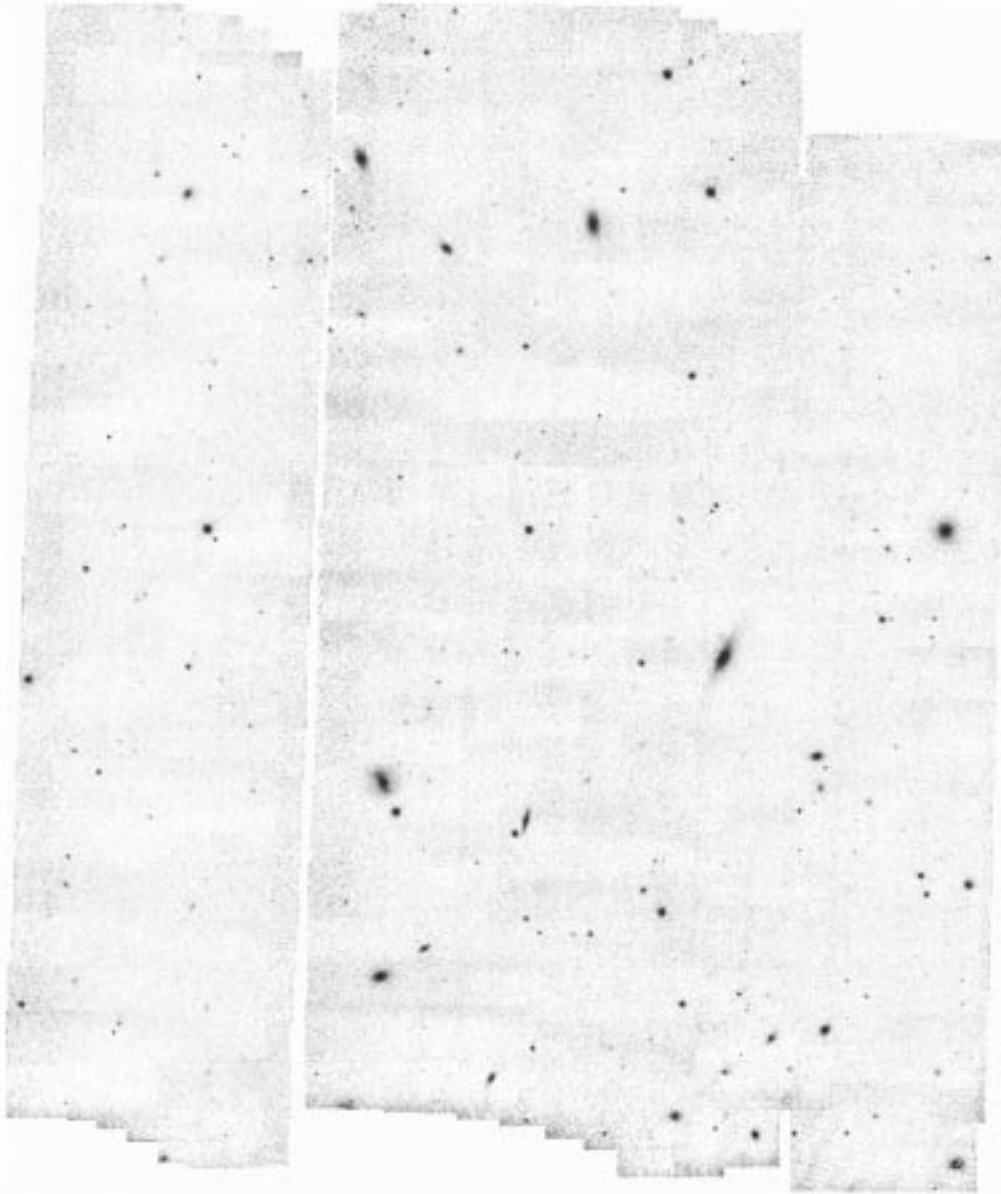


Fig. 1. *H*-band mosaic of the region under investigation. Faint objects have $H \sim 16$ in this heavily rebinned and compressed (for display purposis) image. The field is $\sim 20 \times 24$ arcmin. North is up and East is left. The two dominant galaxies of the Coma cluster are located near the South-West corner

amount of reliable data (photometry *and* morphological types) are already available. We adopted the *H* band because it corresponds to the *K* band – still observable from the ground – for galaxies at intermediate redshift ($z \sim 0.3$), thus allowing a direct comparison of the galaxy properties over a redshift range where evolution in clusters has been detected (Butcher & Oemler 1984). *J*-band (1.2μ) images for the same region have been already acquired and their reduction is in progress.

2. Strategy of observation

The studied region is $\sim 20 \times 24$ arcmin wide, located ~ 15 arcmin North-East from the Coma cluster center (see Fig. 1). The approximate center of the region is 13 00 35 +28 14 35 (J2000). We voluntarily avoided imaging the Coma cluster core, because of the possible presence of a halo around the two dominant galaxies, which would make the reduction and analysis of the data more difficult, given the small field of view of our camera.

Data were taken in the near-infrared *H* band, on March 4th and 9th, and April 3rd to 5th, 1997, at the

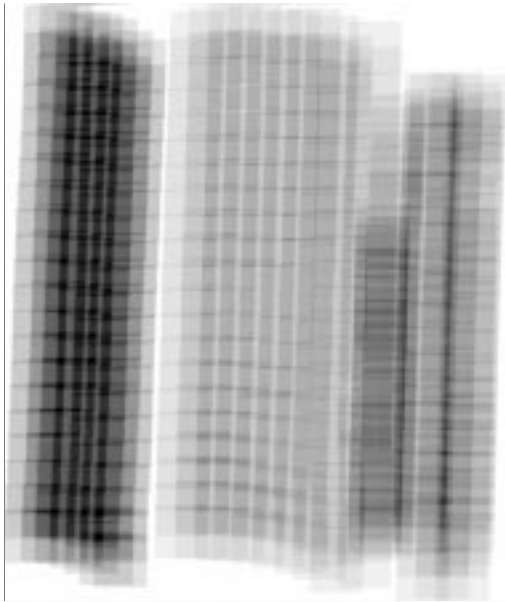


Fig. 2. Exposure map for the whole imaged field (20×24 arcmin wide). North is up and East is left. Darker regions were exposed longer. Exposure times range from 450 s (dark regions), to 0 (white regions). Mean exposure times are, from left to right, 400, 100 and 310 s

2-meter *Télescope Bernard Lyot* of Pic du Midi Observatory (France), with the *Moïcam* camera set at its $f/8$ focus. *Moïcam* is a 256×256 pixel camera, based on an array of 2×2 NICMOS-3 detectors. The adopted configuration gives the maximum field of view available, $2' \times 2'$, with a pixel size of 0.5 arcsec. A few hours per night were allocated to us in March, and half-nights in April.

For an efficient use of the assigned observing time, we did not guide the telescope during the exposures. This limits the individual exposure times to 30 s, without appreciable degradation of the PSF. This is also an optimum value for the exposure time in *H*, in order to reach a suitable signal-to-noise ratio on individual exposures, while keeping the sky background relatively low (~ 3000 to 6000 ADU). In order to image the 20×24 arcmin region with the camera, we mosaicked the total field by successive strips in declination, moving the telescope by half a field of view in declination between exposures, and by half a field of view in right ascension between strips. In this way, with the exception of the regions close to the edge of each field, each point in the sky is observed four times, giving a total exposure time per sky pixel of 120 s.

Almost half of the field was observed more than four times in order to reach fainter magnitudes. This was achieved in three ways: by doubling the number of exposures at each telescope pointing, by moving the telescope by $1/3$ of a field of view instead of $1/2$, or by observing the same strip on different nights. The final median exposure times

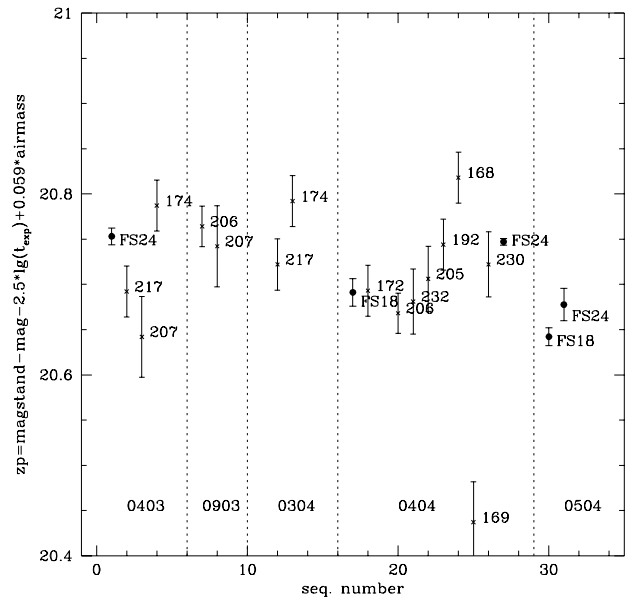


Fig. 3. Magnitude zero point, as measured from standard stars (solid dots) and from Coma cluster galaxies (crosses), splitted by date and then sorted by an arbitrary sequential order. Note that one tickmark along the ordinates is 0.05 mag. Error bars for galaxies account for centering error and published errors of the standard (statistical errors are virtually null for our measure of these bright objects observed for the photometric calibration), whereas for stars they are the ratio of the interquartile range of the various measures by the square root of the number of measures. Labels correspond to names: from Dressler (1980) for galaxies and from Casali & Hawarden (1992) for stars

are 310, 120 and 400 s respectively for the fields patch1 (0403+0903+0304), 0404 and 0504, as were dubbed the regions – from their date of observation.

Unfortunately, the telescope does not point with a precision of one pixel, and therefore, our 675 manually introduced telescope offsets¹ are only approximately achieved on the sky (see Fig. 2). These errors accumulate to create a field which is not exposed in a perfectly uniform way, and, since the actual offset is a few arcsec smaller than the required one and systematic errors accumulate in RA, there are regions exposed more than required and others never exposed. This problem was unknown at the time of the observations, probably because no-one had tried to use our observational strategy before at this telescope (we observed during the very first observing runs with the NICMOS-3 camera). However, since we returned repeatedly to the same regions, only one narrow gap is left in the whole field, between fields 0504 and 0404. Two bright galaxies of Coma fall in this gap, GMP 2413 and GMP 2418, as well as several QSOs and stars.

¹ One every 30 s; we warmly thank the telescope operators for the work involved.

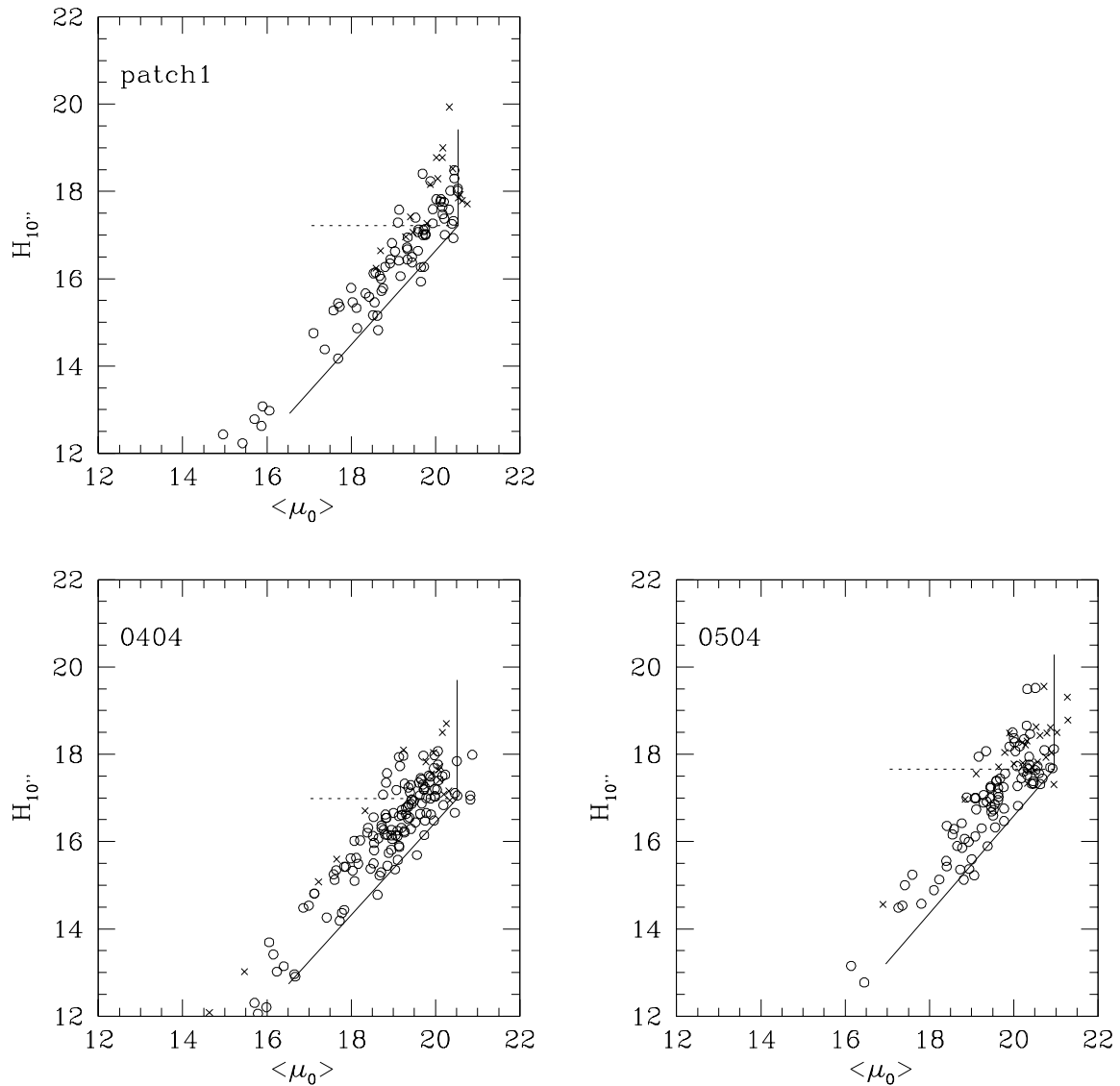


Fig. 4. Average central surface brightness vs. magnitude in a $10''$ aperture for the three fields. The completeness magnitude is indicated by the horizontal dashed line. Circles mark reliable galaxies, crosses objects with uncertain star/galaxy classification ($0.7 < \text{stellarity index} < 0.8$)

All images have been taken with the same exposure time, 30 s, in order to simplify the data reduction.

3. Data reduction

3.1. Dark

The *masterdark* is the median of a stack of 25 individual darks. The rms noise of an individual dark is about 16 to 23 ADU, depending on the NICMOS-3 quadrant. In the *masterdark*, pixels whose intensity differs by more than 70 ADU from the surrounding ones (they are $\sim 1\%$ of the total number of pixels) were replaced by the local average. These pixels were found to show a different behavior from

their neighbors at a low illuminating flux, and a normal behaviour at high illuminating flux (i.e. in calibration and science images).

The gain of the camera was found to be $10 \text{ e}^-/\text{ADU}$.

3.2. Flatfielding

This is a challenging task with near-infrared images, and therefore a detailed description of the way we flatfielded our images is necessary. In the near-infrared, observers are faced with rapid changes of the intensity *and* spectrum of the sky. In the H band, the measured contribution of the telescope and warm-optics background is 80 ADU during

the day (in 30 s, shutter closed), and probably less during the night; this is negligible with respect to the sky level and total background emissivity (shutter open), which is usually ~ 3000 ADU in 30 s. We can therefore apply an “optical reduction” to our *H*-band data.

Our images are quite empty: the majority of the pixels see to the sky most of the times, and the shift between successive exposures is larger than the typical size of objects. Therefore, we decided not to take offset images, and to use the images themselves for flatfielding, thus doubling the time allocated to science frames. The procedure to flatfield our near-infrared images is basically the same as that used for super-flats in the case of optical images.

$$final = (raw - masterdark) / (superflat - masterdark).$$

For each image, the *superflat* is computed as follows:

- a) we consider only images taken not longer before or after the exposure to be flat-fielded;
- b) the median of each image is computed;
- c) we retain only those having a median which differs by less than 5% from that of the image to be flatfielded, with a maximum of 25 images. More liberal limits do not increase the quality of the flatfielding as judged by the flatness of the flattened image. We verified that this choice gives better flatfielded images than taking the temporally nearest 25 (or any number between 9 and 25) images for the creation of the superflat. We interpret the above result as evidence that the spectrum and the intensity of the sky in the near-infrared are correlated. For more than 2/3 of the images, 25 images whose intensities differ by at most 3% were used;
- d) the images are divided by their median;
- e) the superflat is a median, over the stack, of the median normalized images.

3.3. Check of the photometric accuracy of the flatfielding

We checked the correctness of the flatfielding by comparing the apparent flux of photometric standards (and of other observed objects) imaged in the four quadrants (and at different locations in each quadrant). 0.01 mag is the present upper limit of the error determination of any trend between location in the field of view and flux. The global photometric quality of the data is discussed in Sect. 3.7.

3.4. List of bad pixels

We manually created the bad-pixel list. In general, *Moïcam* has an excellent cosmetics, and only a few regions required to be masked: two small (~ 10 -pixel wide) clusters and half a row between two quadrants.

3.5. Sky subtraction

From each flatfielded image we subtracted a constant, the sigma clipped mean computed over the whole image.

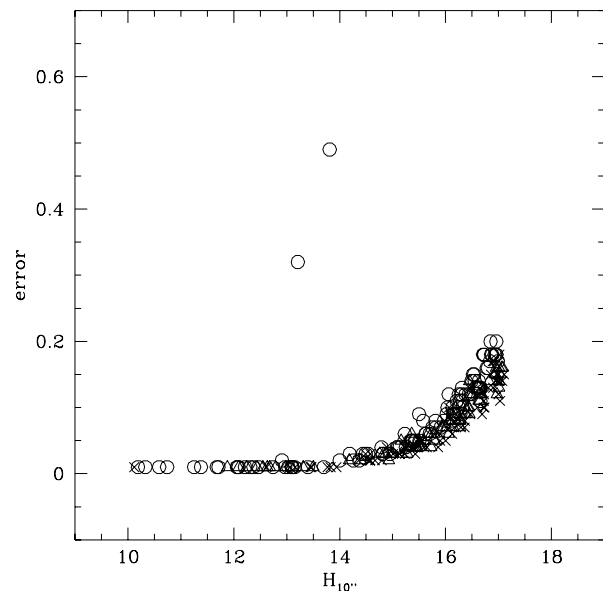


Fig. 5. Magnitude error as a function of the 10'' aperture magnitude for patch1 (triangles), 0404 (circles) and 0504 (crosses). The two outliers are in a noisier than average region, on the border of the region considered for the final catalogue

In passing, we note that the average *H*-band sky brightness during our 5 nights was 14.2 mag arcsec⁻², more than one magnitude fainter than the values typically encountered at other European northern observatories, such as the William Herschel Telescope at La Palma, or at TIRGO on Gornegrat. It is only 0.1 mag brighter than the mean value observed on Mauna Kea.

3.6. Spatial offset

Most images contain at least one bright object which is common to other neighboring images. The angular shifts between the 675 pointings have been computed manually for several reasons. There was no information written on the image-file headers about the position of the telescope when the images were acquired. Besides, when no bright objects are present, allowing one to produce an accurate position of the centroids automatically and blindly, the image have to be recentered manually. This is also the only way to correct for the presence of ghosts and remnant images (arising from extremely bright sources). Fortunately, these events were rare and they were perfectly corrected after the processing.

3.7. Photometric calibration

Standard stars from the UKIRT faint standard list (Casali & Hawarden 1992) were observed once or twice per night. Each standard star was usually exposed four times or

Table 1. Photometric zero point, outside atmosphere, for a 1-s exposure time. The number of objects is given in brackets

Night	Standard stars	Standard galaxies	Adopted zero point
4/3	20.76 (1)	20.69 (3)	20.76
9/3		20.76 (2)	20.76
3/4		20.76 (2)	20.76
4/4	20.71 (2)	20.71 (9)	20.71
5/4	20.67 (2)		20.67

more, at least once per detector quadrant. Figure 3 shows the zero points (solid dots). We supplement these a few measurements by using as standards the Coma galaxies whose magnitudes are listed in Recillas-Cruz et al. (1990). The latter magnitudes are taken with an InSb photometer within a 14.8 arcsec diaphragm and have an average error of 0.02 mag. Of course, in our comparison with Recillas-Cruz et al. (1990) we use 14.8 arcsec aperture magnitude. These zero-point are shows in Fig. 3 as crosses. When stars and galaxies zero-points are available, the agreement is good, as also shows in Table 1.

The field imaged on April 3rd largely overlaps with the field imaged on March 4th and 9th. The magnitudes of the 9 bright objects in the overlapping region are in good agreement, with a typical scatter of 0.03 mag and an average difference of only 0.02 mag, which confirms that these nights were photometric. The fields observed the other nights have too small overlaps to allow a useful comparison in the same way. Nevertheless, all along the recentering procedure, we have checked the consistency of the photometry between different neighboring images of the same bright sources.

Coma was observed through airmasses which differ at most by 0.1 mag. Assuming an atmospheric extinction of 0.059 mag/airmass, the zero-point variation due to airmass variations is at most 0.0059 mag. We neglected this variation (and we assumed an airmass of 1.1 for all observations).

Overall, the agreement between zero points computed from different standard objects (UKIRT stars and Recillas-Cruz et al. (1990) galaxies), the agreement on the magnitude of the same object observed in different nights and the consistency of the photometry of the same object in the various individual 30 s exposures, all these facts suggest us that the zero point error in our photometry is very unlikely to be systematically worse or variable more than 0.02 mag.

3.8. Mosaicking

The images were mosaicked using the task `imcombine` under IRAF. Files containing the flux scaling, the background value, and the relative offsets were given in input. The task gives in output the composite image, the image

of the measured dispersion among the input images, the number of pixels used (i.e. the exposure map in units of 30 s). The expected variance of the composite image has been computed from these quantities, assuming standard laws for the propagation of errors.

The task `imcombine` has a number of tunable parameters whose setting affects the results. Since we split the desired exposure time into shorter exposures, we composited the images by averaging the fluxes measured in the different images, as we would have done if ideal conditions (low sky flux, perfect NICMOS-3 cosmetics, good telescope tracking) were met. We allowed the exclusion of up to 2 values for each sky direction in order to remove cosmic rays and transient hot pixels. We verified that other schemes (such as taking a median, or a sigma clipped average possibly centered on the median, etc.) do not conserve the flux of the objects within our images (many objects are sufficiently exposed, even when for only 30 s, for accurately measuring their magnitudes and comparing them with those measured on mosaicked images). The reason is that the average of a distribution has the useful characteristic, by definition, to be equal to the integral of the distribution divided by the number of data points. The median, or any other elaborate means of computing the central location of a distribution (in particular when it is formed by a small number of points, as our one) does not have such property and therefore does not conserve the integral of the distribution (the total flux), which is the scientific interesting quantity.

In the mosaicking, we started by compositing the images on a night by night basis. We checked the relative photometry and astrometry first between the composite image and the parent single 30-s images, then among nights when possible. This careful check allowed us to detect mistakes and systematic errors: displacement errors appear in regions of particularly high sigma, when the error is small, or as regions of under-average exposure time with respect to those of the same RA, when errors are large. Photometric errors (due for example to an incorrect setting of the `imcombine` task), appear quite clearly, for example as a good agreement between fluxes of the same object imaged in different 30-s exposures, but as a discrepant flux in the composite image (or in the image of another night).

In the final image, the seeing is ~ 1.7 arcsec *FWHM*, of which we estimate that ~ 0.5 arcsec have been added during the data reduction, and with variations (0.5 arcsec) from region to region.

3.9. Astrometry

In order to provide accurate positions for the objects in our three fields, we used the astrometric catalog of the USNO version 1 (Monet et al. 1999). In the three composite near-infrared images there are significant (> 2 arcsec)

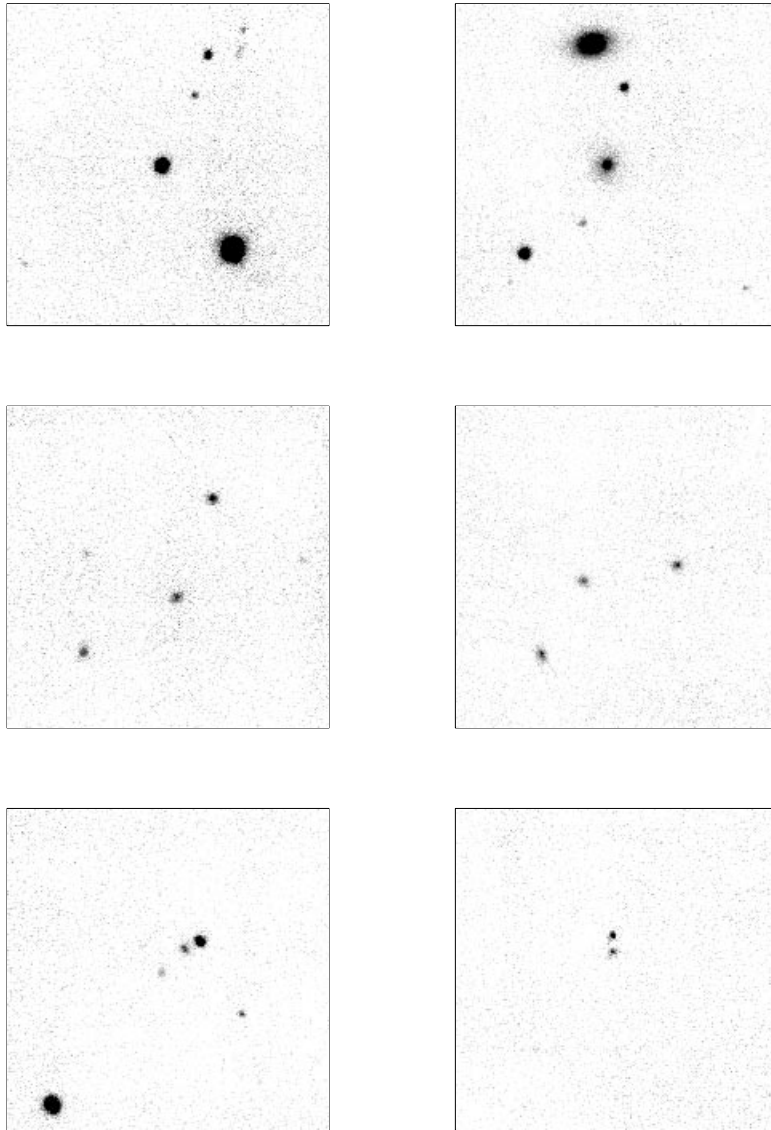


Fig. 6. A zoom on a few objects. Faint galaxies in the lower panels have $H \sim 17$

astrometric distortions (i.e. significant deviations from a linear relation between relative positions measured on our composite images and the actual positions on the sky). Therefore, we first established an approximate conversion from the positions of the objects in our three fields to the USNO using the task `geomap` in IRAF. We projected our field (represented as in Fig. 7), with the appropriate shifts in RA and DEC, on a red image of the field, taken from the Second Digitized Sky Survey (hereafter POSS-II). Then, we associated objects having similar sizes, ellipticities, position angles and sky positions in our Fig. 7 and on the POSS-II. Most near-infrared objects fall within 2 arcsec of their optical counterpart. Finally, we adopted as coordinates for the near-infrared objects the POSS-II coordinates of the corresponding optical objects (which correspond to epoch 1993.4, date of the POSS-II plate)

and preprocessed them to J2000 using the USNO catalog. The final accuracy of the absolute position is 1 arcsec, given by the quadratic sum of the accuracy of the USNO and the scatter observed in the conversion from POSS-II to USNO coordinates.

A few (~ 10) objects, out of ~ 300 , are fainter than the limiting magnitude of the POSS-II, and their positions are therefore accurate to a few arcsec.

3.10. Detection & completeness

For the tasks of detection and photometry, we applied Sextractor (version 2) (Bertin & Arnouts 1996) to our images and rms map. To be detected, objects should have 9 pixels brighter than 1σ on both the filtered (by a Sex

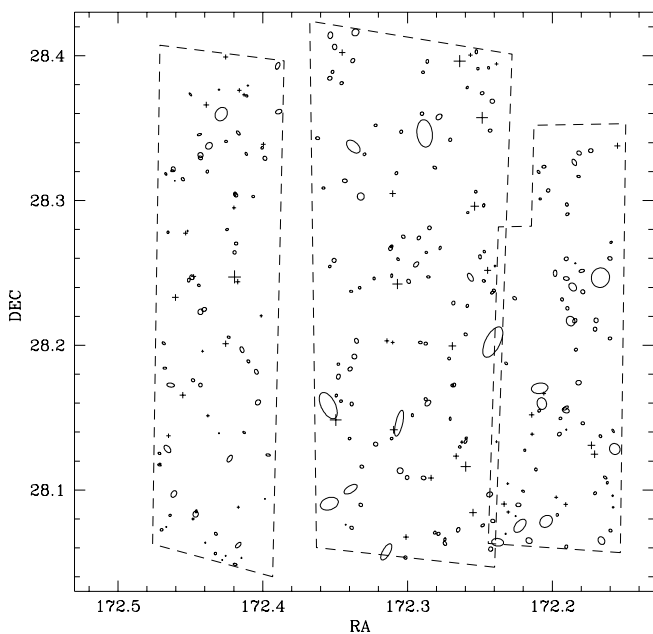


Fig. 7. Detected objects brighter than the completeness magnitude. Crosses are stars, ellipses are galaxies. The area of ellipses is twice the $22 \text{ mag arcsec}^{-2}$ isophotal area. The dashed lines delimit the regions covered by the final catalogue. Coordinates are J2000. For simplicity of display, right ascension is given as $\alpha \times 15 \times \cos 28^\circ$

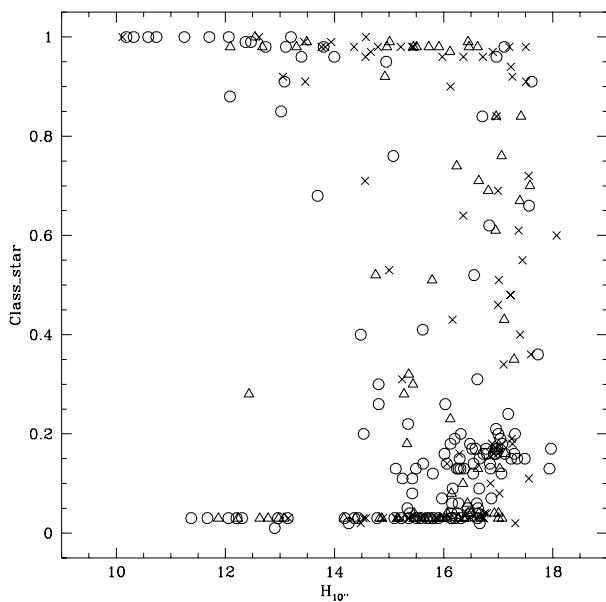


Fig. 8. Classification parameter as a function of the $10''$ aperture magnitude for patch1 (triangles), 0404 (circles) and 0504 (crosses)

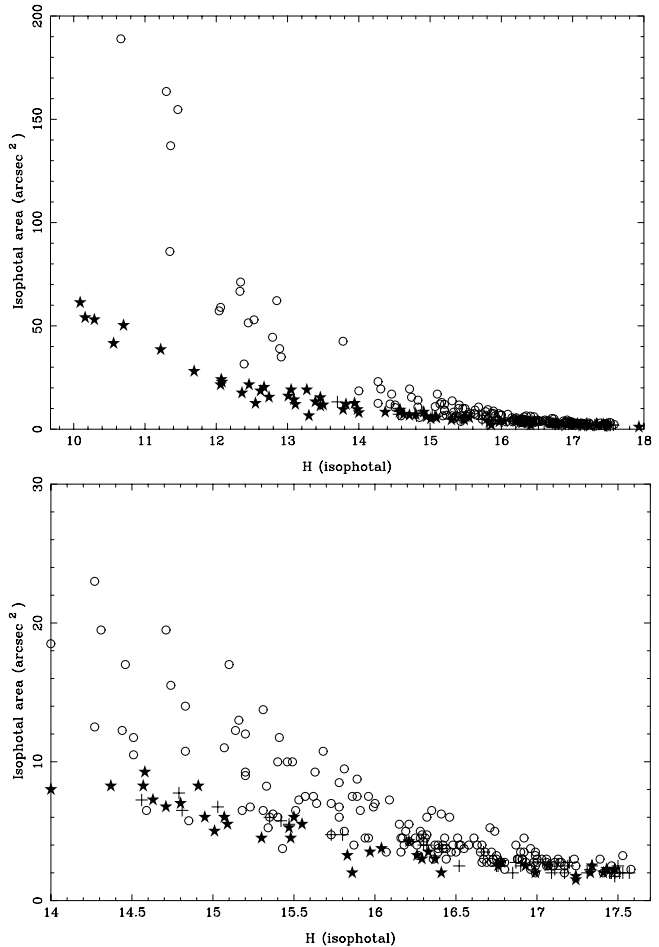


Fig. 9. Isophotal area (in arcsec^2) versus isophotal magnitude (corresponding to $\mu = 22 \text{ mag arcsec}^{-2}$) in the whole field studied. Objects identified as stars are shown as black stars, whereas objects identified as galaxies or unclassified objects are displayed as open circles and crosses, respectively

standard “all-ground” convolution mask with $FWHM = 2$ pixels) and the unfiltered image.

Inside each field, the exposure time and the noise properties do not change enough to affect the probability of detection of the objects considered in this paper, except near the edge of the field, a region which is hereafter excluded from the analysis. The final useful area is 380 arcmin^2 ; the region excluded because on the border is $\sim 40 \text{ arcmin}^2$.

The completeness was computed in each field as described in Garilli et al. (1999). In brief, objects are detected when their central surface brightness (not their magnitude) is brighter than the detection threshold. Objects with a given central surface brightness may have different magnitudes. The completeness magnitude at a given central brightness is taken as the brightest magnitude of the objects having such central surface brightness (see Fig. 4).

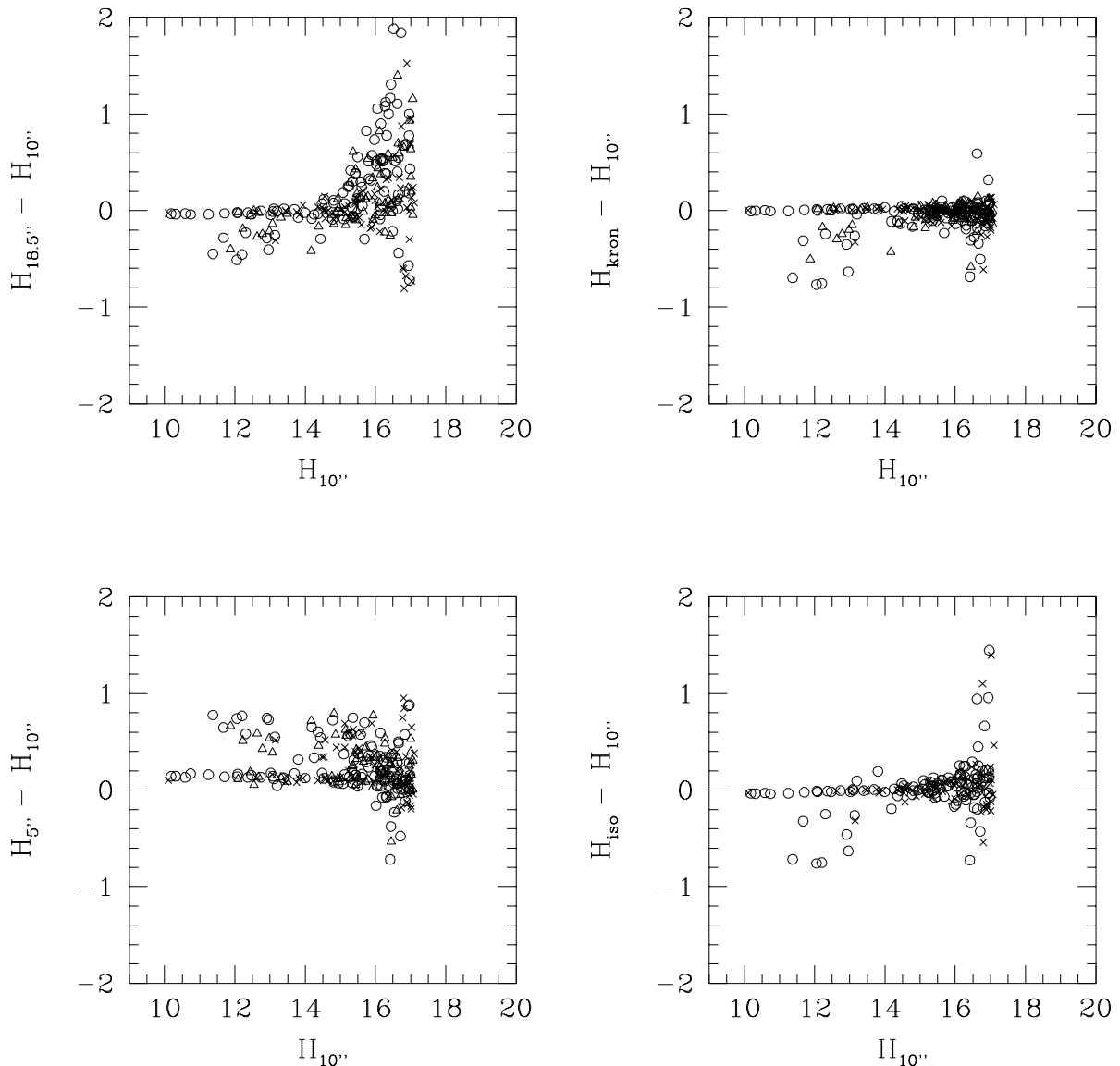


Fig. 10. Residual magnitude vs. magnitude diagrams for patch1 (triangles), 0404 (circles) and 0504 (crosses) for objects brighter than the $H_{10''}$ completeness magnitude. The scatter is due to variety of surface brightness radial profiles of objects in the studied region. Note that Kron and $H_{10''}$ magnitudes are quite similar at $H_{10''} \sim 14$

Detected objects in the last half-magnitude bin have typically $S/N \sim 5$ (see Fig. 5). A note of caution: due to the large number of operations performed on the data and the complex way we do it, magnitude errors could be non strictly poissonian (or Gaussian) in nature, and therefore it could happen that the error distribution has broader wings than a Gaussian.

Table 2 shows the completeness magnitudes for several types of magnitudes.

Table 2. Nominal completeness magnitudes

type	patch1	0404	0504
mag _{iso}	17.2	16.9	17.2
mag _{kron}	17.2	17.0	17.2
mag _{5''}	17.4	17.2	17.4
mag _{10''}	17.1	17.0	17.2
mag _{13''}	16.9	17.8	17.9
mag _{14.5''}	16.8	16.8	16.8
mag _{18.5''}	16.5	16.5	16.5

4. Results

Tables 3, 4 and 5 (given only in electronic form) present the extensive photometry in the near-infrared H band of

a sample which is complete in all the types of magnitudes listed in Table 2, in an area of about 400 arcmin² toward the Coma cluster of galaxies. Figures 1 and 7 show the

studied region and the detected objects. An important point to mention is that $H \sim 17$ mag is six magnitudes below the characteristic magnitude of galaxies, well into the dwarfs' regime at the distance of the Coma cluster. To our knowledge, this is the first *complete* sample of galaxies in a nearby cluster for which the photometry is published.

Figure 8 shows the classification parameter as a function of $H_{10''}$. According to the SExtractor criteria, the classification is secured for most objects in this field, at least down to the completeness magnitude. When $Class_star < \sim 0.3$, objects are identified as galaxies, whereas $Class_star > \sim 0.7$ (for 0404 and 0504) and $Class_star > \sim 0.8$ (for patch1) correspond to stars. The difference between fields is due to seeing conditions.

Figure 9 displays the result of this classification when comparing the isophotal area (at $\mu = 22$ mag arcsec $^{-2}$) to the corresponding isophotal magnitude. Stars and galaxies easily separate in two different sequences in a large magnitude range. This visual criterion is similar to the one originally proposed by Godwin & Peach (1977). The difference between the two sequences tends to vanish at faint magnitudes. In our case, the separation between stars and galaxies seems to be reliable down to the completeness limit.

Figure 10 shows a comparison between the different magnitudes obtained in this field. As expected, magnitudes are sensitive to the size of the apertures for bright objects ($H \lesssim 14$), and apertures larger than $\sim 10''$ give similar results for $H \gtrsim 14$.

Tables 3, 4 and 5 give, for each object brighter than at least one of the limits indicated in Table 2:

- sky coordinates (epoch J2000);
- H -band magnitude within the apertures: $5''$, $10''$, $13''$, $14.5''$ and $18.5''$, and their errors, as computed by Sex. Listed errors do not include photometric zero-point errors (see Sect. 3.7), those arising from the compositing, and implicitly assume a gaussian or poissonian error distribution;
- isophotal ($\mu = 22$ mag arcsec $^{-2}$) and Kron magnitudes (with errors). Kron magnitudes are computed by integrating the flux in an area 2.5 times larger than the Kron area, with a minimum aperture radius of 1.8 arcsec. “9.99” or “99.99” means that no measure is available (usually because the object is too small or too faint for its flux to be measured through a large aperture);
- isophotal area (at $\mu = 22$ mag arcsec $^{-2}$), in arcsec;
- ellipticity and position angle (from North to East);
- Kron radius, or 1.8 arcsec if the latter is larger;
- stellarity index as defined by SExtractor;
- an optical identification, usually taken from the Godwin, Metcalfe & Peach (1983, and private communication).

This catalogue is the database used to compute the luminosity function in this field (Andreon & Roser, in press), and also to study the morphology and the photometric properties of these galaxies in details.

Acknowledgements. We thank Alain Klotz for obtaining our March data the TBL. We also thank the TBL technical staff for their support during the observing runs. The USNO catalog and the POSS image were obtained at the Canadian Astronomy Data Center (CADDC), which is operated by the Herzberg Institute of Astrophysics, National Research Council of Canada.

References

- Andreon S., Pelló R., 1999, A&A (in press)
- Bertin E., Arnouts S., 1996, A&AS 117, 393
- Barger A.J., Aragon-Salamanca A., Ellis R.S., et al., 1996, MNRAS 279, 1
- Butcher H.R., Oemler A. Jr., 1984, ApJ 285, 426
- Casali M., Hawarden T., 1992, JCMT-UKIRT Newslett. 3, 33
- Cowie L.L., Songaila A., Hu E.M., Cohen J.G., 1996, AJ 112, 839
- de Lapparent V., Galaz G., Arnouts S., Bardelli S., Ramella M., 1997, The Messenger 89, 21
- De Propriis R., Eisenhardt P., Stanford S.A., Dickinson M., 1998, ApJ 503, L45
- Dressler A., 1980, ApJS 42, 565
- Gardner J.P., Sharples R.M., Frenk C.S., Carrasco B.E., 1997, ApJ 480, L99
- Garilli B., Maccagni D., Andreon S., 1999, A&A 342, 408
- Godwin J.G., Metcalfe N., Peach J.V., 1983, MNRAS 202, 113
- Godwin J.G., Peach J.V., 1977, MNRAS 181, 323
- Monet D., Bird A., Canzian B., et al., 1999, The USNO -A1 guide star catalog, Washington DC, US Naval Observatory
- Pahre M.A., Djorgovski S.G., De Carvalho R.R., 1998, AJ 116, 1591
- Petrosian V., 1998, ApJ 507, 1
- Recillas-Cruz E., Carrasco L., Serrano A., et al., 1990, A&A 229, 64
- Saracco P., Chincarini G., Iovino A., 1996, MNRAS 283, 865
- Szokoly G.P., Subbarao M.U., Connolly A.J., Mobasher B., 1998, ApJ 492, 452
- Trentham N., Mobasher B., 1998, MNRAS 299, 488